In Situ Measurement of Multistep Anodic Aluminum Oxide Fabrication for Quartz Crystal Microbalance-based Sensing Applications

Brandon Murray, Xuanjie Wang, Shankar Narayan*
Department of Mechanical, Aerospace, and Nuclear Engineering,
Rensselaer Polytechnic Institute, 110 8th Street, Troy, NY 12180
*Corresponding author. E-mail address: narays5@rpi.edu. Telephone: 1-518-276-6988
|Contributed equally.

Abstract

Ordered nanostructures on a quartz crystal microbalance (QCM) can be used to develop sensors for various applications, including frosting and icing. Since nanostructures with a specific geometry are often desirable for sensing, this work focuses on using the two-step anodization of aluminum to obtain a well-organized, tunable pore array on a QCM. More importantly, this study analyzes the fabrication process of a nanoporous anodic alumina array using a QCM *in situ*. Where frequent geometric characterization of nanopores during fabrication can be challenging, sometimes destructive, and often requiring interruption to the fabrication process, the QCM-based approach developed here can be used throughout the fabrication process without much interruption. The QCM frequency and resistance measured and analyzed during fabrication can determine the structure of the pores while they are being fabricated. The QCM-determined pore structure compared with images using a scanning electron microscope, empirical correlations, and anodization current show agreement. The *in situ* measurement using QCM serves as a guideline to template surfaces for sensing frosting and icing processes.

Keywords

Quartz Crystal Microbalance, Anodic Aluminum Oxide, Porous Alumina, Nanostructures, Melting, Freezing

1. Introduction

Frosting and icing exist widely in refrigeration and cryogenics fields and often adversely affect airflow, heat transfer, and power generation. The in-depth studies on dynamic characteristics and underlying mechanisms of frosting and icing have fundamental significance. Conventional frosting studies quantify the dynamic process using visualization tools and real-time mass detection, but the accuracy is limited to macroscale sensing [1–4]. In addition, since freezing is affected by surface morphology and wettability, typical optical techniques are not suitable for monitoring phase change on a surface with nanostructures. Therefore, an alternative technique with sensitive measurements is required.

A quartz crystal microbalance (QCM) consists of a quartz crystal substrate with patterned electrodes whose resonant frequency changes based on the stress applied on the electrode surface.

Data acquisition of QCM's resonant frequency with a resolution of 1 Hz is possible with standard instrumentation, yielding a mass sensitivity close to 18 ng/cm². Hence, while QCMs have traditionally monitored thin-film deposition [5], they have also been used to study a wide range of surface phenomena, including liquid-vapor interfacial characteristics and wetting phenomena [6–36]. It is also possible to measure simultaneously thin solid and liquid films, which is a clear benefit for frosting and icing research compared to traditional mass or heat balance methods [17,36–39]. QCMs can also be precise droplet contact area sensors for studying evaporation [28,30,34,40] and have shown promise as sensors for frosting and icing [41–43].

Anodic aluminum oxide (AAO) is a common template for creating ordered nanostructures for semiconductors, optics, water desalination, and biomedical sensing due to the self-organized and tunable geometry achievable with relatively simple fabrication processes [44–47]. Masuda et al. first reported the two-step anodizing process of AAO to yield an ordered array [48]. Since then, by choosing proper anodization conditions, researchers have found that the hexagonal close-packed arrangement (Figure 1) could be adjusted to result in a wide range of pore diameters (10-400 nm) and pore densities (10⁸-10¹⁰ pores/cm²) [49].

Sensing applications often need nanostructures with specific dimensions [50–54]. Nanostructures built directly on QCMs have been used to design humidity [55–60] and gas sensors [53,61–67], biosensors [68], mercury sensors [69], study surface wettability [33,70,71], solvent infiltration [72], droplet impact dynamics [73], and determine fluid properties [74] and sorption isotherms [51,75]. A tunable and highly ordered nanoporous alumina can be grown on a QCM with aluminum coatings. The tunable structure provides a versatile method to template surfaces for frosting and icing since freezing is affected by surface morphology and wettability [76]. Besides using AAO-integrated QCM as a sensor, it can also be a template to make ordered nanostructures (e.g., nano-posts or cylinders) on QCM with metallic, polymeric, and ceramic materials, which can serve specific needs for general sensing applications [77–81]. As a tunable template, the change in AAO geometry (Figure 1), including the pore diameter, interpore distance, pore height, pore wall, and barrier layer thickness, is closely related to the type of electrolytes, applied voltage, duration, and temperature during fabrication. It is necessary to investigate the growth process of tunable nanostructure using a highly sensitive and accurate method.

Monitoring the AAO fabrication process is crucial to achieving the desired nanostructures at high throughput. While previous studies provide empirical guidelines, wherein some variation in structure is possible due to differences in fabrication setups and control conditions, QCM presents the unique capability and advantage of monitoring nanostructure fabrication to tailor the process and obtain the desired nanopore geometry. In this study, the *in situ* measurement of the AAO structure during the fabrication process carried out can provide new insights into geometry control. Although the anodization process to obtain AAO can be analyzed using applied potential and current measurements, a QCM gives additional insight into the rate of pore formation and pore geometry. Further, wet chemical etching processes during nanopore fabrication, which do not have any voltage or current data, can also be monitored using the QCM, providing the tunability of pore structure in real-time. The *in situ* measurement by QCM allows monitoring of the evolution of geometry and serves as a guideline to template surfaces for sensing applications.

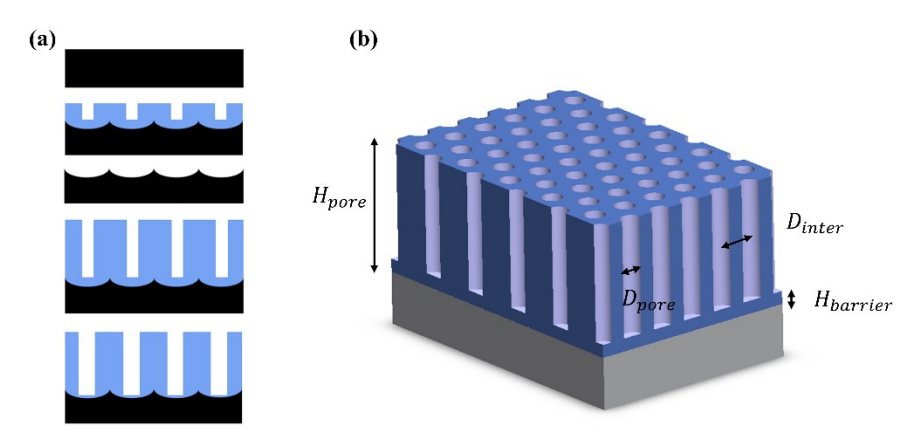


Figure 1: (a) Fabrication process of ordered anodic alumina oxide (AAO) using two-step anodization, chemical etching, and pore-widening processes. (b) Schematic of highly ordered AAO nanopores with key geometric parameters.

2. QCM Analysis of AAO Fabrication Process

2.1 AAO Fabrication

The QCM used in this work was a 25.4 mm diameter, 5 MHz AT-cut crystal with a nominally 10 µm thick aluminum (99.99% Al) electrode. AAO is created on the QCM using standard electrochemical techniques [82]. A two-step anodization process uses oxalic acid with chemical etching using chromic and phosphoric acids, resulting in hexagonally ordered nanopores (Figure 1). Specifically, the first anodization was carried out in 0.3 M oxalic acid to form AAO. Then, the AAO was etched away in a mixture of 1 wt.% chromic acid and 6 wt.% phosphoric acid. The anodization process was repeated under similar conditions to form AAO in a hexagonal pattern. Subsequently, a pore-widening process was carried out with 1 wt.% phosphoric acid (Figure 1). Table 1 summarizes the fabrication process where the second anodization was performed in three consecutive steps of 80, 78, and 110 minutes, a total of 268 minutes. Each fabrication step was performed with the QCM inserted into a temperature-controlled solution bath (double jacket beaker) with a magnetic stir and temperature probe (Figure 2). After each fabrication step, the QCM was rinsed with deionized water. The same temperature-controlled bath was used for the QCM characterization measurements.

Table 1: Summary of the fabrication process

Step	Solution	Time	Temperature	Voltage
First Anodization	0.3 M Oxalic Acid	50 min	2 °C	40 V
Etching	1 wt.% Chromic +	50 min	32 °C	-
	6 wt.% Phosphoric Acid			
Second Anodization	0.3 M Oxalic Acid	268 min	2 °C	40 V
Pore Widening	1 wt.% Phosphoric Acid	30 min	30 °C	-

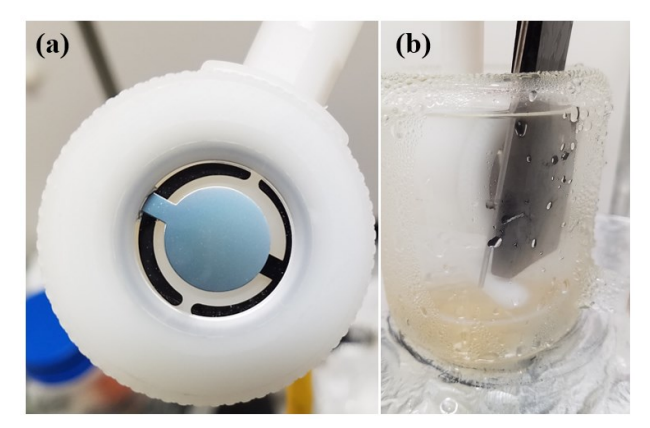


Figure 2: (a) Aluminum-coated QCM in a holder. (b) QCM was inserted into an anodization cell with a temperature probe, graphite electrode, and magnetic stirrer.

2.2 QCM Overview

Film thickness on the QCM's surface is typically determined using Sauerbrey's equation:

$$\Delta f = -C_f \frac{\Delta m}{A_q} \tag{1}$$

This equation describes the linear relationship between the frequency shift, $\Delta f = f - f_0$ and the areal mass, $\Delta m/A_q$ on the QCM. Here, f is the resonant frequency, f_0 is the unloaded resonant frequency, Δm is the mass change over the electro-active area of the QCM (A_q) . The proportionality constant, C_f is the mass sensitivity, which depends on f_0 and quartz material constants. C_f has a theoretical value of 56.6 Hz.cm²/ μ g for a 5 MHz QCM. For rigid thin films, only the areal mass density is measurable in the frequency response. For thick films, the acoustic properties of the films are relevant. However, this is only the case when the frequency response exceeds 5% of the unloaded frequency ($\Delta f/f > 0.05$). In this work, the frequency response due to inertial mass load is small, $\Delta f/f < 0.005$, so only rigid thin films need to be considered.

While Eq. (1) is suitable for rigid layers, it does not apply to a QCM loaded with a fluid. The oscillation of the QCM surface causes fluid motion adjacent to it, which decays exponentially from the crystal surface. This decay length, related to fluid density (ρ_f) and viscosity (μ_f), is given by $\delta = (\mu_f/\pi f \rho_f)^{1/2}$. Within a distance of δ , which is ~240 nm for water on a 5 MHz QCM crystal, the motion decays by 63%. The frequency shift of a QCM exposed to a Newtonian fluid is given by Eq. (2a) [83,84]. Additionally, the fluid on the QCM surface damps the motion of the crystal, and this can be measured by a change in resistance of the QCM circuit, ΔR [85]. An increase in ΔR is proportional to a decrease in the quality factor of oscillation. ΔR is related to ρ_f and μ_f , as shown in Eq. (2b) [85].

$$\Delta f = -C_f \sqrt{\frac{\rho_f \mu_f}{4\pi f_0}} \tag{2a}$$

$$\Delta R = 2L_1 C_f \sqrt{\frac{\pi \rho_f \mu_f}{f_0}} \tag{2b}$$

Here, the unloaded motional inductance of the QCM is L_1 , which is on the order of ~40 mH, as shown later. ΔR is directly measurable using standard equipment (e.g., SRS QCM200 - Stanford Research Systems, used in this work).

The effects of rigid mass loads (Eq. (1)) and liquid damping (Eq. 2(a)) are additive to the frequency response of the QCM. Previous works have studied the effect of liquids on rough surfaces and porous structures on the QCM frequency [37,38,74]. Notably, the liquid in the nanopores behaves as an effective mass, follows Saurbrey's equation (Eq. (1)), and does not cause a damping effect. The additive frequency response is then shown in Eq. (3).

$$\Delta f = -C_f \left(\phi h \rho_f + \sqrt{\frac{\rho_f \mu_f}{4\pi f_0}} \right) \tag{3}$$

Here, the mass change is replaced by $\Delta m = \phi h \rho_f$, where the fluid (of density ρ_f) fills the pores of porosity, ϕ , and height, h.

It should be noted that the resonant frequency of a QCM can be affected by temperature changes during measurement. When submerged in a solution, the main drivers of QCM response are the density and viscosity of the fluid, which are functions of temperature. For water around room temperature, the sensitivity of frequency and resistance response (Eq. 2) is around 8 Hz/°C and 4 Ω /°C, respectively, based on fluid properties and theoretical QCM constants. This work considers the temperature-dependent fluid properties at each measurement time in the data analysis to compensate for temperature fluctuations. In addition, the properties of quartz material that determine the unloaded resonant frequency are affected by temperature. The QCM chosen for this work, an AT-cut crystal (Fil-Tech), is optimized for use around 25 °C, with < 25 Hz frequency response when heated to 70 °C. This variation is neglected in this work since it is about 400 times smaller than the ~10 kHz measured responses.

This study used a 1 sample per second measurement rate for QCM frequency and resistance measurements. Data acquired at this rate can be considered real-time without any sensor delays because fluid damping and mass loading are stress-based phenomena on the QCM, and the time constant of these responses would be similar to the crystal's oscillation period.

2.3 QCM Analysis of AAO Fabrication

Formation of the Barrier Layer: The fabrication process can be analyzed by considering the changes in mass over the crystal surface. During the anodization processes, first, the barrier layer (h_{BL}) grows to a height of ~52 nm [86], replacing aluminum (Al) with alumina (Al_2O_3) and expanding volumetrically, increasing the mass of the QCM by $\Delta m = A_q \left(h_{BL_{Al_2O_3}} \rho_{Al_2O_3} - h_{BL_{Al}} \rho_{Al} \right)$, where h and ρ denote thickness and density, respectively. As pores form, the fluid mass in the pores must also be considered. The porosity can be written in terms of the pore cross-sectional area to the electro-active QCM area, $\phi = A_{cs}/A_q$. The mass change during pore creation can be written as $\Delta m/A_q = \phi \rho_f \Delta h_{Al_2O_3} + (1-\phi)\rho_{Al_2O_3} \Delta h_{Al_2O_3} + \rho_{Al}\Delta h_{Al}$. The total fluid

damping load (Eq. (2b)) does not change during anodization, thereby not contributing to the frequency response of the QCM.

Anodization Steps: The frequency shift, $\Delta f = f - f_o$ during the anodization processes is given by Eq. (4), where the unloaded frequency (f_o) corresponds to the QCM submerged in the anodization bath before the barrier layer forms, and the loaded frequency (f) corresponds to measurements at any time during anodization. If Δf is calculated between two points after barrier layer formation and the QCM is submerged in the same liquid, then $h_{BL_{Al_2O_3}} = h_{BL_{Al}} = 0$, which further simplifies Eq. (4).

$$\Delta f = -C_f \left(\phi \rho_f \Delta h_{Al_2O_3} + (1 - \phi) \rho_{Al_2O_3} \Delta h_{Al_2O_3} + \rho_{Al} \Delta h_{Al} + \rho_{Al_2O_3} h_{BL_{Al_2O_3}} - \rho_{Al} h_{BL_{Al}} \right) (4)$$

Here, $\Delta h_{Al_2O_3}$ and Δh_{Al} are the changes in alumina and aluminum thicknesses, respectively. Since the oxide expands faster than aluminum consumption, $\Delta h_{Al_2O_3}$ and Δh_{Al} are not equal.

Pore Etching and Widening Steps: The pore walls, the top, and the bottom surfaces are dissolved slowly during the etching step. The change in mass from the dissolution in the vertical direction is $\Delta m/A_q = \rho_{Al_2O_3}\Delta h_{Al_2O_3}$. In the radial direction, the pore wall is replaced by the fluid at a constant pore height, which corresponds to a change in mass of $\Delta m/A_q = \phi_i h_{Al_2O_{3i}} \left(\frac{r^2}{r_i^2} - 1\right) \left(\rho_f - \rho_{Al_2O_3}\right)$ where r is the radius of the pore. Assuming isotropic etching, the total distance etched in the vertical and radial directions is identical. Hence, $\Delta h_{Al_2O_3} = r_i - r$. Consequently, the frequency response of the QCM is given by

$$\Delta f = -C_f \left(\rho_{Al_2O_3}(r_i - r) + \phi_i h_{Al_2O_{3i}} \left(\frac{r^2}{r_i^2} - 1 \right) \left(\rho_f - \rho_{Al_2O_3} \right) \right)$$
 (5)

Here again, $\Delta f = f - f_o$ where the "unloaded" frequency (f_o) corresponds to the QCM just submerged in the etching solution, and the final frequency (f) is any time during the etching process. Note that Δf in Eq. (5) only depends on densities and the initial geometry (porosity, ϕ_i , radius, r_i , and height, $h_{Al_2O_{3i}}$).

While complete etching of pores is performed between the first and second anodization steps, partial etching or pore widening would use the same analytical procedure. During complete etching of pores, Eq. (5) is valid only until the barrier layer is etched, exposing the aluminum substrate. Beyond this stage, the nanopores detach from QCM and collapse in the etchant. Equations (4) and (5) can determine the rate of pore growth, total pore height, and porosity of the anodic alumina nanopore structure by measuring the frequency response of the QCM during the fabrication process and is an alternative to visual methods done intermittently or at the end of fabrication.

3. Results

3.1 Determining L_1 and C_f for QCM

The value of L_1 and C_f are determined by submerging the QCM into various non-reactive fluids with a wide range of densities and viscosities (Table 2). These solutions are used as standards to characterize the mass and damping response of the specific crystal used in this work to provide

reliable pore measurements. This step, carried out after each fabrication step, tracks the pore geometry without affecting the structure. The QCM was rinsed with DI water and blown dry with nitrogen gas between each solution. This step is also critical to ensure the QCM is clean and free of contaminants before proceeding to the next fabrication step.

Table 2: Com	norican of	f dancities or	d viceocities	a of fluide u	god for I	determination at 25°	20
Table 2. Com	parison or	uchsines ai	ia viscositici	o or munus u	iscu for L_1	ucteriiiiiaiioii at 23	

	n-Hexane	IPA	Water	15 wt.%	45 wt.%	3M Novec TM
	[87]	[87]	[88]	Glycerol [88]	Glycerol [88]	7000 [89]
Density, g/m ³	655	781	997	1033	1110	1401
Viscosity, mPa.s	0.3	2.04	0.893	1.315	3.919	0.445

Eq. (6), derived using Eq. (2b) and Eq. (3), and replacing the pore height, $h_{Al_2O_3}$ with $\dot{h}_{Al_2O_3}t$, where t is the anodization time (Table 1), gives the growth rate of the pores, $\dot{h}_{Al_2O_3}$, during anodization. $\dot{h}_{Al_2O_3}$ is a good estimate of the average growth rate since the pores grow at a rate independent of pore height for anodization performed under fixed conditions.

$$-\frac{\Delta f}{\Delta R} = C_f \phi \dot{h}_{Al_2O_3} \frac{\rho_f t}{\Delta R} + \frac{1}{4\pi L_1} \tag{6}$$

The frequency and resistance shifts were analyzed with linear-least-squares fits to Eqs. (2b) and (6), as shown in Figure 3, to obtain L_1 and C_f .

Figure 3(a) is a plot for Eq. (6) with $\Delta f/\Delta R$ versus $\rho_f t/\Delta R$ using data from all the fabrication steps, which collapses onto two distinct lines. One of these lines corresponds to the "after pore widening" data, and the other corresponds to the remaining data from all other steps. The intercept of the line with the majority dataset $(1/4\pi L_1)$ gives L_1 . The slope of this equation, $C_f \phi \dot{h}_{Al_2O_3}$, is related to C_f and the pore geometry $(\phi \dot{h}_{Al_2O_3})$. In this case, the slope is 0.00041 s⁻²m³/kg, and the intercept is 1.867 H⁻¹, which gives $L_1 = 42.6$ mH. The second line in Figure 3(a), denoting data recorded after pore widening, shows a different slope compared to the majority of data. This difference is due to the porosity change by a factor of ~2.5, evident from the ratio of the slopes. Here, L_1 is determined from the majority data set because it has a robust y-intercept, whereas the pore-widening data requires extrapolation.

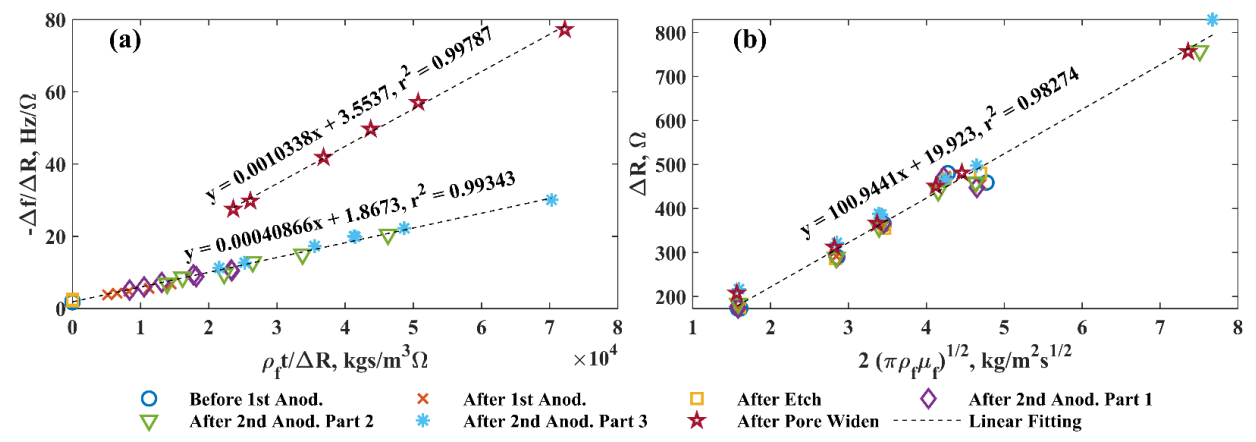


Figure 3: Linear fitting of frequency and resistance data to find motional inductance (L_1) and mass sensitivity (C_f) . Eq. (6) is used in (a) and Eq. (2b) in (b).

Figure 3(b) is a plot for Eq. (2b) with ΔR versus $2\sqrt{\pi\rho_f\mu_f}$, where the slope is $L_1C_ff_0^{-1/2}$. The best-fit line to the entire experimental dataset has a slope of $100.94~\mathrm{H~s^{-3/2}~m^2~kg^{-1}}$. A reasonable value for C_f can be found by taking L_1 to be 42.6 mH and assuming f_0 to be 5 MHz (manufacturer data), giving $C_f = 53.0~\mathrm{Hz~cm^2/\mu g}$, which is very close to the theoretical value of $56.6~\mathrm{Hz~cm^2/\mu g}$. Using this value of C_f , the value of $\phi \dot{h}_{Al_2O_3}$ is 4.63 nm/min. Porosity and rate can be separately determined using standard methods of pore analysis or from the fabrication data, as explained later. Note that the "after pore widening data" does not show a different trend for ΔR in Figure 3(b), indicating that the resistance measurement (Eq. (2b)) is independent of pore geometry, which is expected. Based on the goodness-of-fit (r^2) in Figure 3 indicating the agreement with the theory, the method used here to determine L_1 and C_f is satisfactory. However, there is more than one way to obtain L_1 and C_f and every crystal is unique, as such the values should be determined for each crystal.

3.2 Determining Pore Geometry

The total mass change after each fabrication step is evaluated based on the frequency shift. By measuring the mean frequency of the clean samples before and after a fabrication step, the difference corresponds to the net areal mass change on the QCM surface ($\Delta f = -C_f \Delta m/A_q$), as shown in Table 3.

Table 3: Frequency shifts and corresponding areal mass change after each fabrication step

	1 st	Etching	2 nd Anod.	2 nd Anod.	2 nd Anod.	Pore
	Anod		Part 1	Part 2	Part 3	Widening
Frequency Shift, kHz	-7.504	29.721	-12.241	-11.220	-13.925	27.952
Mass Change, μg/cm ²	141.7	-561.1	231.1	211.8	262.9	-527.7

Using the frequency shifts from all the fabrication steps, excluding pore widening, in Eq. (4), and assuming all the changes in alumina and aluminum heights proportional to the anodization time, a set of five linear equations can be created with the unknowns $\dot{h}_{Al_2O_3}$, \dot{h}_{Al} , $h_{BL_{Al_2O_3}}$, $h_{BL_{Al}}$, and ϕ . Note that C_f and $\phi \dot{h}_{Al_2O_3}$ are already computed. This system of equations is solved using linear least-squares optimization to obtain $\dot{h}_{Al_2O_3}=42.2$ nm/min, $\dot{h}_{Al}=-30.4$ nm/min, $h_{BL_{Al_2O_3}}=91$ nm, and a porosity of $\phi=0.11$.

The barrier layer thickness of 91 nm is in the same order of magnitude as previous results [86,90]. In addition, extrapolation of the pore growth rate from Hwang *et al.* [82] at 2 °C gives 44 nm/min, and Sousa *et al.* [91] at 4 °C gives 41.7 nm/min, which is quite close to the 42.2 nm/min determined here at 2 °C. The summary of pore heights after each fabrication step is given in Table 4. Here, the pore heights are calculated from the pore growth rate $(\dot{h}_{Al_2O_3})$ and the anodization time. The aluminum substrate's final height is zero because the substrate was almost entirely consumed, and the substrate height was calculated based on the aluminum consumption rate (\dot{h}_{Al}) and anodization time.

Table 4: Pore and estimated substrate heights after each fabrication step based on fabrication time and calculated growth/consumption rate.

	Unmodified	1st Anod.	Etching	2 nd Anod.	2 nd Anod.	2 nd Anod.	Pore
				Part 1	Part 2	Part 3	Widening
Pore Height,	0	2.11	0	3.38	6.67	11.3	11.3
$h_{Al_2O_3}$ (µm)							
Est. Substrate	9.65	8.13	8.13	5.71	3.34	~0	~0
Height, h_{Al} (μ m)							

3.3 Frequency and Resistance Response during Anodization

The first anodization was performed in 0.3M oxalic acid at around 2 °C and 40 V for 50 minutes (Figure 1). Figure 4 shows the frequency response of the QCM during the anodization process, which shows three distinct regions: (1) a nearly constant frequency prior to submersion in the oxalic acid, (2) a steady rate of decrease in frequency, and (3) a relatively constant frequency occurring after the QCM was removed from the acid bath and dried in N₂ gas. The frequency decrease corresponds to Eq. (4), where adding oxygen molecules to make alumina and immersion in oxalic acid reduces the frequency.

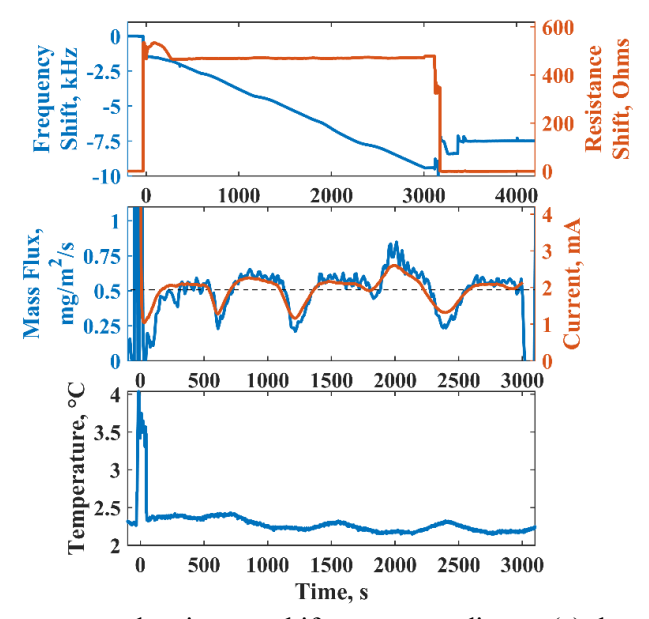


Figure 4: (Top row) Frequency and resistance shifts corresponding to (a) the unloaded QCM in the air prior to submersion, (b) in oxalic acid throughout anodization, and (c) a final period outside the bath and in air. (Middle row) Mass flux of the crystal surface, current, and (bottom row) acid temperature recorded during the anodization process. The average mass flux is shown as the black dashed line. Anodization voltage was applied at time zero.

Three distinct regions are also seen in the QCM resistance response. Here, the middle region plateaus rather than decreases. This plateau in *R* is because the addition of fluid in the nanopores plays no role in Eq. (2b). The fluid moves rigidly within the nanopores and provides no damping. When the QCM returns to the ambient air condition at the end of the anodization process, the resistance returns to its original value. The resistance fluctuates slightly during early anodization since the bath temperature is not strictly constant. Small temperature changes can produce

measurable viscosity and density changes of oxalic acid, affecting the resistance. The temperature is relatively constant during anodization, except when the QCM and its holder are submerged just before time zero. The large thermal mass of the holder temporarily warms the acid bath before a recirculating cooler returns the bath to the desired set point. The initial transient period corresponds to the QCM holder and oxalic acid coming to equilibrium.

In order to determine the rate of mass addition to the QCM during the anodization process, Eq. (2b) can be combined with Eq. (4) to eliminate the fluid viscosity, and the time derivative of this expression results in Eq. (7).

$$\dot{m}'' = -\frac{1}{C_f} \frac{d}{dt} \left(\frac{\Delta R}{4\pi L_1} + \Delta f \right) = \left(\phi \left(\rho_f - \rho_{Al_2O_3} \right) + \rho_{Al_2O_3} \right) \dot{h}_{Al_2O_3} + \rho_{Al} \dot{h}_{Al}$$
 (7)

Here, the mass flux, \dot{m}'' , which indicates the mass addition per unit area per unit time, can be found directly from the resistance and frequency measurements. When extended to physical densities and the pore structure, the right-hand term comprises the consumption of pure aluminum and the creation of alumina nanopores filled with oxalic acid. This quantity should show the same trends as the electric current measured in the electrochemical cell, as indicated in Figure 4. The oscillatory behavior is likely from temperature fluctuations of the anodization cell.

Based on the average growth rates of alumina, the consumption rate of aluminum, porosity, the values of C_f and L_1 , an average mass flux can be determined from the right-hand side of Eq. (7). The dashed black horizontal line shows the average mass flux in Figure 4. The right-hand side of Eq. (7)'s agreement with the derivative-based data is exceptional. In addition to the QCM, the measured current can determine the growth rate of the pores. By conservation of charge, $\dot{h}_{Al_2O_3} = m_{Al}I/3A_qe\rho_{Al}$, where m_{Al} is the mass of an aluminum atom, I is current, and e is the charge of an electron (1.602 × 10⁻¹⁹ C). With an average current of 2 mA and electrode area of 1.29 cm², the current-calculated growth rate would be 32.2 nm/min. Although the current-calculated growth rate is slightly lower than the QCM-calculated rate, they are in close agreement. This comparison demonstrates the applicability of these equations to describe fabrication phenomena occurring in nanopores on a QCM. Identical results can be seen for the second anodization step, which is not included here for conciseness.

3.4 Frequency and Resistance during Etching

Like the first anodization step, chromic and phosphoric etching can be analyzed in terms of its mass flux, shown in Eq. (8).

$$\dot{m}'' = -\frac{1}{C_f} \frac{d}{dt} \left(\frac{\Delta R}{4\pi L_1} + \Delta f \right) = \left(h_{Al_2O_{3i}} \phi_i \frac{2r}{r_i^2} (\rho_f - \rho_{Al_2O_3}) - \rho_{Al_2O_3} \right) \frac{dr}{dt}$$
(8)

Unlike anodization, the mass flux in this step depends on the radius as a function of time. Due to the small dimensions involved ($r_i \sim 10$ nm), the leading term of the right-hand side is much larger than the density of alumina and dominates the mass flux, that is $\dot{m}'' \propto -r \frac{dr}{dt}$.

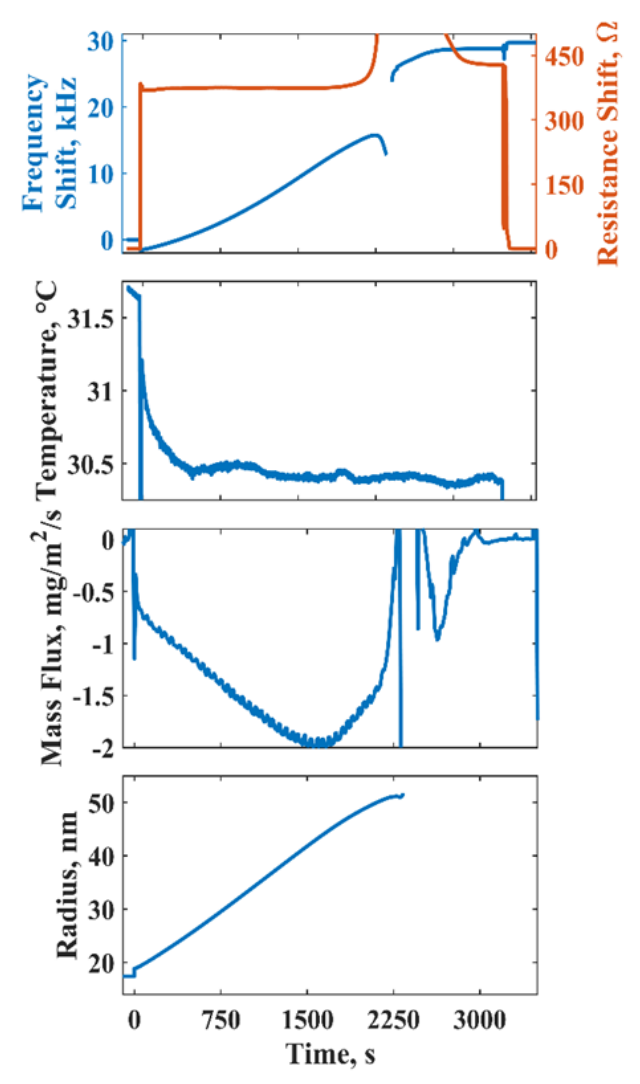


Figure 5: Frequency and resistance shifts from unloaded in-air crystal prior to submersion in chromic-phosphoric acid recorded throughout etching with the final period outside the acid bath, in the air. The mass flux of the crystal surface and temperature of the acid were recorded during the etch process, and QCM was submerged at time zero. A significant break in data around 2250 seconds is attributed to pore wall collapse. Here, Eq. (5) was used to calculate the radius.

Figure 5 shows the QCM response during the etching step that removes the pores after the first anodization. As noted earlier, data analysis becomes impossible when the pores collapse after 2250 seconds. At this point, the frequency and resistance responses reach non-physical values as the QCM undergoes a rapid change in stress. However, once this stress subsides, the measurements return to practical values. After 2500 seconds, there must be macro-scale features in the remaining alumina because the resistance measurement is elevated from its nominal value during the majority of the etching process, and there must be some additional fluid undergoing a damped shear wave motion. At close to 3400 seconds, the frequency and resistance stop changing, which implies that the etching of alumina is complete. The chromic-phosphoric etchant is selective; hence, it does not affect the aluminum substrate.

After etching, the QCM shows a nearly 30 kHz frequency change in the air. This significant change corresponds to pore removal with the associated aluminum and oxygen atoms, which is larger than the -7.5 kHz change in Figure 4. Although oxygen atoms are added to the QCM during anodization, only a small net loss of aluminum occurs during anodization. The balance (\sim 22.2 kHz), when used in Eq. (1) with aluminum density, indicates that an aluminum layer of \sim 1.52 μ m was consumed during the first anodization-etch process.

Equation (8) is best applied in the 0 to 2000 seconds interval when the pore structure still exists. The mass flux shows a linearly decreasing trend before increasing. The negative value here indicates that mass is lost from the QCM surface, in line with the etching process. The linear increase in the magnitude of mass flux could mean the radius is increasing linearly if dr/dt = constant or non-linearly if $dr/dt \neq$ constant. After 1500 seconds, the rate's decreasing magnitude (increasing value) shows something interesting occurs when the pore walls have become very thin. However, currently, we do not know why this might be happening. From around 3000-3500 seconds, the mass flux approaches zero as etching is completed and no alumina remains. Variations (ripples) in the mass flux are attributed to tiny local temperature fluctuations and fluctuations from the stir bar in the etchant bath.

The radius of the pore can be determined using Eq. (5). The initial porosity is used to determine the initial radius using the interpore spacing, a = 100 nm (Figure 7 and Ref. [82]), where $r_i = a\sqrt[4]{3}\sqrt{\phi/2\pi} = 17.4$ nm. The calculated radius shows a linear trend until about 2200 seconds. Above this time, Eq. (5) does not represent the pore structure well. At 2394 seconds, the calculated radius reaches a maximum local value of 51.2 nm to the close-packing limit of 50 nm for a 100 nm interpore spacing. Any etching past 50 nm in a perfectly ordered cylindrical array would rupture pore walls. Here, 51.2 nm is within the margin of error, and pore walls have likely begun to rupture. Once enough pores have been combined, the frequency will decrease because the fluid will no longer act as a rigid mass while increasing the damping on the QCM. Above 2400 seconds, the damping measurement (resistance) and frequency show these trends.

Pore widening is similar to the etching step. However, a lower acid concentration is used to limit the etch rate to obtain the desired pore radius. The parameters for pore widening (Figure 6) can be calculated using the same equations and analysis used for the etching step. The insertion of the QCM into the pore-widening acid results in a downward frequency shift as liquid enters the pores. And then, as with the etching step, frequency increases as the pore walls are etched and replaced with fluid. Finally, a large increase in frequency occurs when the QCM is removed from the liquid and dried in the air. The final frequency is larger than the initial frequency (before pore widening) because the pores have grown in radius. The mass flux during the pore widening step follows the same trend seen in the etching step - both show a slowly increasing magnitude of mass flux with time due to the higher diffusion rate of reactant and product species as the pores become wide.

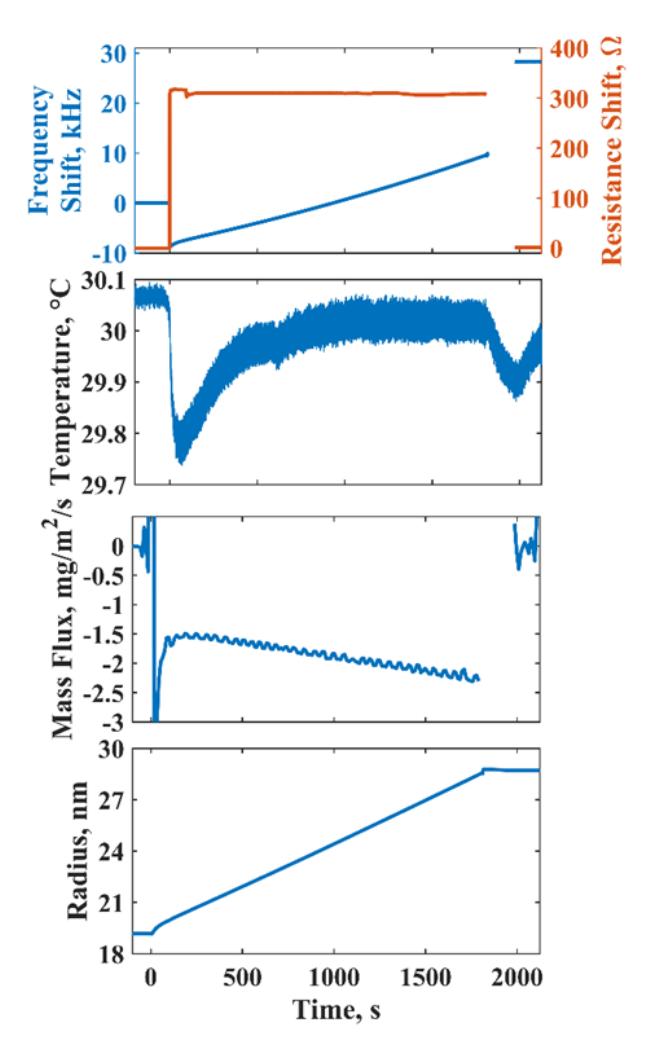


Figure 6: Frequency and resistance shifts from unloaded in-air crystal prior to submersion in phosphoric acid recorded during pore widening with the final period outside the acid bath in the air. Mass flux of the crystal surface and temperature of the acid were recorded during the pore widening process, and QCM was submerged at time zero. A significant break in data around 1900 seconds is when the QCM is removed from the bath, rinsed, and dried. Here, Eq. (5) was used to calculate the radius.

3.5 Pore Imaging

The morphologies of the fabricated QCM were characterized after the final anodization process using high-resolution scanning electron microscopy (Zeiss 1540ESB Crossbeam SEM), as shown in Figure 7(a-b) and (d-e). In these images, an ordered pore surface can be seen with an interpore separation of 95-105 nm. The pore diameter distributions and porosity were measured using the ImageJ software, as shown in Figure 7(c, f). Specifically, with a threshold of 12.24%, where the whitest pixels were set to white, and the remainder were set to black, we obtained a binary image indicating a porosity of 0.14. Only regions larger than 200 square pixels were counted for the pore area. As shown in Figure 7(c), the average pore diameters for QCM before pore widening were 37.9 ± 4.3 nm with a porosity of 0.14, which agrees with the QCM calculated radius of 18 nm and porosity of 0.14. The pore size distribution after pore widening is shown in Figure 7(f), where the

average pore diameter is 57 ± 4.6 nm, and the porosity is 0.29, which is also in agreement with the QCM calculated radius of 28.6 nm and porosity of 0.3 (Figure 6).

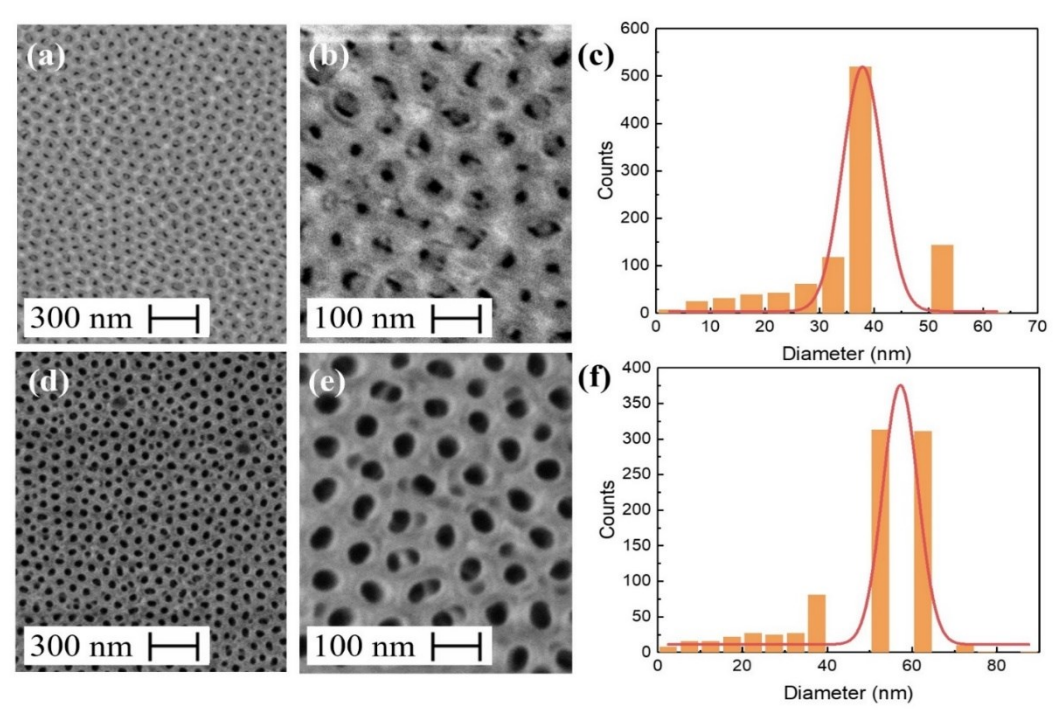


Figure 7: SEM image of nanoporous QCM before pore widening (after anodization) at 100X (a) and 300X (b) magnification. SEM image of the same QCM after pore widening (after anodization) at 100X (c) and 300X (d) magnification. Pore size distributions of QCM before (c) and after pore widening (f).

4. Conclusions

Anodic alumina nanopores were fabricated and analyzed in this work using a QCM. The fabrication was performed in a multistep process with a first anodization step to create ordered initiation sites, followed by etching, and second anodization to create a highly ordered array of parallel cylindrical pores, followed by pore widening to obtain the desired pore diameter. The QCM allowed for high-precision measurements *in situ* during fabrication, which conventional techniques cannot achieve. The QCM measurements were in excellent agreement with other standard approaches (e.g., SEM, current measurements) and empirical relations in the literature.

Frequency and resistance measurements taken during fabrication in solutions of varying density and viscosity characterize the pore geometry. Equations were derived from the theory that liquid inside oscillating nanopores will undergo rigid in-phase motion, unlike semi-infinite fluids near the oscillating QCM surface. These relations accurately predict the porosity and pore geometry of the QCM when compared with the SEM images. Additionally, the pore growth rate and height were determined non-destructively. Further, Eqs. (2b) and (3) apply over various pore heights and fluid properties. The analysis presented here will help advance nanostructure-integrated QCM as a high-precision sensor for various applications and study different phenomena occurring in the nanoscale, including frosting and icing.

5. Acknowledgments

The work was supported by the National Science Foundation's Division of Chemical, Bioengineering, Environmental, and Transport Systems in the Directorate for Engineering under Grant No. 1944323.

6. CRediT Authorship Contribution Statement

B.M. and X.W. contributed equally to this work.

Brandon Murray: Methodology, Investigation, Writing-original draft, Visualization, Formal analysis.

Xuanjie Wang: Methodology, Investigation, Writing-original draft, Visualization, Formal analysis.

Shankar Narayan: Supervision, Methodology, Writing-review and editing, Project administration, Funding acquisition.

7. References:

- [1] M. Song, X. Wang, L. Liao, S. Deng, Termination Control Temperature Study for an Air Source Heat Pump Unit during Its Reverse Cycle Defrosting, Energy Procedia. 105 (2017) 335–342.
- [2] M. Song, S. Deng, C. Dang, N. Mao, Z. Wang, Review on improvement for air source heat pump units during frosting and defrosting, Appl. Energy. 211 (2018) 1150–1170.
- [3] M. Song, C. Dang, T. Higashi, E. Hihara, Review of experimental data associated with the solidification characteristics of water droplets on a cold plate surface at the early frosting stage, Energy Build. 223 (2020) 110103.
- [4] L. Zhang, M. Song, S. Deng, J. Shen, C. Dang, Frosting mechanism and behaviors on surfaces with simple geometries: A state-of-the-art literature review, Appl. Therm. Eng. 215 (2022) 118984.
- [5] G. Sauerbrey, Verwendung von Schwingquarzen zur Wägung dünner Schichten und zur Mikrowägung, Zeitschrift Für Phys. 155 (1959) 206–222.
- [6] Q. Chen, S. Xu, Q. Liu, J. Masliyah, Z. Xu, QCM-d study of nanoparticle interactions, Adv. Colloid Interface Sci. 233 (2016) 94–114.
- [7] G.N.M. Ferreira, A.C. da-Silva, B. Tomé, Acoustic wave biosensors: physical models and biological applications of quartz crystal microbalance, Trends Biotechnol. 27 (2009) 689–697.
- [8] H. Zhuang, P. Lu, S.P. Lim, H.P. Lee, Frequency response of a quartz crystal microbalance loaded by liquid drops, Langmuir. 23 (2007) 7392–7397.
- [9] Z. Lin, M.D. Ward, Determination of Contact Angles and Surface Tensions with the Quartz Crystal Microbalance, Anal. Chem. 68 (1996) 1285–1291.
- [10] J.W. Lin, S.K. Fan, Real time contact angle measurement by quartz crystal microbalance

- for EWOD studies, 2010 IEEE 5th Int. Conf. Nano/Micro Eng. Mol. Syst. NEMS 2010. (2010) 325–328.
- [11] K.D. Esmeryan, G. McHale, C.L. Trabi, N.R. Geraldi, M.I. Newton, Manipulated wettability of a superhydrophobic quartz crystal microbalance through electrowetting, J. Phys. D. Appl. Phys. 46 (2013) 1–9.
- [12] S.Y. Kwon, J.C. Kim, B. Il Choi, Recognition of supercooled dew in a quartz crystal microbalance dew-point sensor by slip phenomena, Metrologia. 44 (2007) L37–L40.
- [13] Y. Xue, Y. Wu, X. Pei, H. Duan, Q. Xue, F. Zhou, How solid-liquid adhesive property regulates liquid slippage on solid surfaces?, Langmuir. 31 (2015) 226–232.
- [14] H. Zhuang, P. Lu, P.L. Siak, P.L. Heow, Effects of interface slip and viscoelasticity on the dynamic response of droplet quartz crystal microbalances, Anal. Chem. 80 (2008) 7347–7353.
- [15] H. Zhuang, H.P. Lee, S.P. Lim, Dynamic response of quartz crystal microbalances in contact with silicone oil droplets, in: C. Quan, K. Qian, A.K. Asundi, F.S. Chau (Eds.), Fourth Int. Conf. Exp. Mech., 2009: p. 75222X.
- [16] G. McHale, P. Roach, C.R. Evans, N.J. Shirtcliffe, S.J. Elliott, M.I. Newton, Sensor response of superhydrophobic quartz crystal resonators, in: 2008 IEEE Int. Freq. Control Symp. FCS, IEEE, 2008: pp. 698–704.
- [17] P. Roach, G. McHale, C.R. Evans, N.J. Shirtcliffe, M.I. Newton, Decoupling of the liquid response of a superhydrophobic quartz crystal microbalance, Langmuir. 23 (2007) 9823–9830.
- [18] H. Zhuang, P. Lu, S.P. Lim, H.P. Lee, Study of the evaporation of colloidal suspension droplets with the quartz crystal microbalance, Langmuir. 24 (2008) 8373–8378.
- [19] J.E. Pye, C.E. Wood, J.C. Burton, Precursors to Molecular Slip on Smooth Hydrophobic Surfaces, Phys. Rev. Lett. 121 (2018).
- [20] J. Su, M. Charmchi, H. Sun, A Study of Drop-Microstructured Surface Interactions during Dropwise Condensation with Quartz Crystal Microbalance, Sci. Rep. 6 (2016) 1–11.
- [21] A. Saluja, D.S. Kalonia, Measurement of fluid viscosity at microliter volumes using quartz impedance analysis, AAPS PharmSciTech. 5 (2004) 68–81.
- [22] D.C. Ash, M.J. Joyce, C. Barnes, C.J. Booth, A.C. Jefferies, Viscosity measurement of industrial oils using the droplet quartz crystal microbalance, Meas. Sci. Technol. 14 (2003) 1955–1962.
- [23] X.H. Huang, W. Pan, J.G. Hu, Q.S. Bai, The Exploration and Confirmation of the Maximum Mass Sensitivity of Quartz Crystal Microbalance, IEEE Trans. Ultrason. Ferroelectr. Freq. Control. 65 (2018) 1888–1892.
- [24] Z. Lin, M.D. Ward, Determination of Contact Angles and Surface Tension with the Quartz Crystal Microbalance, Anal. Chem. 68 (1996) 1285–1291.
- [25] H. Zhuang, S.P. Lim, H.P. Lee, Effects of compressional waves on the response of quartz

- crystal microbalance in contact with silicone oil droplets, J. Appl. Phys. 105 (2009) 1993.
- [26] Q. Bai, J. Hu, X. Huang, H. Huang, Using QCM for field measurement of liquid viscosities in a novel mass-sensitivity-base method, in: 2016 IEEE Int. Freq. Control Symp. IFCS 2016 Proc., IEEE, New Orleans, LA, USA, 2016: pp. 1–3.
- [27] Z. Lin, M.D. Ward, The Role of Longitudinal Waves in Quartz Crystal Microbalance Applications in Liquids, Anal. Chem. 67 (1995) 685–693.
- [28] B. Murray, S. Narayanan, The Role of Wettability on the Response of a Quartz Crystal Microbalance Loaded with a Sessile Droplet, Sci. Rep. 9 (2019) 1–13.
- [29] G. Couturier, S. Vatinel, R. Boisgard, J.P. Aim, A. Chabli, Quartz crystal microbalance and evaporation of sessile droplets, J. Appl. Phys. 106 (2009) 054906.
- [30] B. Murray, M.J. Fox, S. Narayan, Analyzing interfacial transport for water evaporating into dry nitrogen, Appl. Therm. Eng. 202 (2022) 117910.
- [31] N.T. Pham, G. McHale, M.I. Newton, B.J. Carroll, S.M. Rowan, Application of the quartz crystal microbalance to the evaporation of colloidal suspension droplets, Langmuir. 20 (2004) 841–847.
- [32] M.J. Joyce, P. Todaro, R. Penfold, S.N. Port, J.A.W. May, C. Barnes, A.J. Peyton, Evaporation of sessile drops: Application of the quartz crystal microbalance, Langmuir. 16 (2000) 4024–4033.
- [33] M. Lee, W. Kim, S. Lee, S. Baek, K. Yong, S. Jeon, Water droplet evaporation from sticky superhydrophobic surfaces, Appl. Phys. Lett. 111 (2017).
- [34] B. Murray, M.J. Fox, S. Narayanan, Quantifying the evaporation rate of sessile droplets using a quartz crystal microbalance, J. Appl. Phys. 128 (2020) 035101.
- [35] Z. Lin, R.M. Hill, H.T. Davis, M.D. Ward, Determination of Wetting Velocities of Surfactant Superspreaders with the Quartz Crystal Microbalance, Langmuir. 10 (1994) 4060–4068.
- [36] Z. Lin, T. Stoebe, R.M. Hill, H.T. Davis, M.D. Ward, Improved accuracy in dynamic quartz crystal microbalance measurements of surfactant enhanced spreading, Langmuir. 12 (1996) 345–347.
- [37] P. Schön, R. Michalek, L. Walder, Liquid density response of a quartz crystal microbalance modified with mesoporous titanium dioxide, Anal. Chem. 71 (1999) 3305–3310.
- [38] S.J. Martin, G.C. Frye, K.O. Wessendorf, Sensing liquid properties with thickness-shear mode resonators, Sensors Actuators A. Phys. 44 (1994) 209–218.
- [39] I. Goubaidoulline, J. Reuber, F. Merz, D. Johannsmann, Simultaneous determination of density and viscosity of liquids based on quartz-crystal resonators covered with nanoporous alumina, J. Appl. Phys. 98 (2005) 1–5.
- [40] X. Li, B. Murray, S. Narayan, Investigation of sessile droplet evaporation using a transient two-step moving mesh model, Int. J. Heat Mass Transf. 209 (2023) 124151.

- [41] K.D. Esmeryan, C.E. Castano, R. Mohammadi, Y. Lazarov, E.I. Radeva, Delayed condensation and frost formation on superhydrophobic carbon soot coatings by controlling the presence of hydrophilic active sites, J. Phys. D. Appl. Phys. 51 (2018).
- [42] K.D. Esmeryan, N.I. Stoimenov, Studying the bulk and contour ice nucleation of water droplets via quartz crystal microbalances, Micromachines. 12 (2021) 1–13.
- [43] H. Ye, Q. Hu, Y. Qi, X. Zhi, L. Qiu, Real-time mass detection of trace water vapor frosting on a cryogenic surface based on quartz crystal Microbalance (QCM) sensor, Appl. Therm. Eng. 230 (2023) 120785.
- [44] X. Wang, M.-L. Hsieh, J.A. Bur, S.-Y. Lin, S. Narayanan, Capillary-driven solar-thermal water desalination using a porous selective absorber, Mater. Today Energy. 17 (2020) 100453.
- [45] X. Wang, M.-L. Hsieh, J.A. Bur, S.-Y. Lin, S. Narayanan, The Role of Nanostructure Morphology of Nickel-Infused Alumina on Solar-Thermal Energy Conversion, J. Opt. (2020).
- [46] X. Wang, H. Yang, M. Hsieh, J.A. Bur, S.-Y. Lin, S. Narayanan, Nickel-Infused Nanoporous Alumina as Tunable Solar Absorber, MRS Adv. 5 (2020) 2575–2583.
- [47] X. Wang, L.V. Repolho Cagliari, J.E. Hicken, S. Narayan, Optimization of nickel-infused alumina nanostructure for enhanced solar-thermal conversion, MRS Commun. 13 (2023) 581–586.
- [48] H. Masuda, M. Satoh, Fabrication of gold nanodot array using anodic porous alumina as an evaporation mask, Japanese J. Appl. Physics, Part 2 Lett. 35 (1996) L126–L129.
- [49] W. Lee, S.-J. Park, Porous Anodic Aluminum Oxide: Anodization and Templated Synthesis of Functional Nanostructures, Chem. Rev. 114 (2014) 7487–7556.
- [50] N. Asai, T. Shimizu, S. Shingubara, T. Ito, Fabrication of highly sensitive QCM sensor using AAO nanoholes and its application in biosensing, Sensors Actuators B Chem. 276 (2018) 534–539.
- [51] M. Beggiato, R. Rastogi, C. Dupont-Gillain, S. Krishnamoorthy, Confined adsorption within nanopatterns as generic means to drive high adsorption efficiencies on affinity sensors, Sensors Actuators B Chem. 366 (2022) 131945.
- [52] A. Shayganpour, M. Salerno, B. Salis, S. Dante, Towards a single bioactive substrate combining SERS-effect and drug release control based on thin anodic porous alumina coated with gold and with lipid bilayers, MRS Adv. 2 (2017) 1597–1604.
- [53] Z. Kang, D. Zhang, T. Li, X. Liu, X. Song, Polydopamine-modified SnO2 nanofiber composite coated QCM gas sensor for high-performance formaldehyde sensing, Sensors Actuators B Chem. 345 (2021) 130299.
- [54] D. Zhou, Z. Kang, X. Liu, W. Yan, H. Cai, J. Xu, D. Zhang, High sensitivity ammonia QCM sensor based on ZnO nanoflower assisted cellulose acetate-polyaniline composite nanofibers, Sensors Actuators B Chem. 392 (2023) 134072.

- [55] D. Zhang, X. Song, Z. Wang, H. Chen, Ultra-highly sensitive humidity sensing by polydopamine/graphene oxide nanostructure on quartz crystal microbalance, Appl. Surf. Sci. 538 (2021) 147816.
- [56] Q. Chen, Y. Yao, X. Huang, D. Liu, K. Mao, Simulation analysis and experimental verification for sensitivity of IDE-QCM humidity sensors, Sensors Actuators B Chem. 341 (2021) 129992.
- [57] N. Yamamoto, T. Yamaguchi, K. Hara, Development of QCM humidity sensors using anodized alumina film, Electron. Commun. Japan. 102 (2019) 39–46.
- [58] D. Zhang, H. Chen, X. Zhou, D. Wang, Y. Jin, S. Yu, In-situ polymerization of metal organic frameworks-derived ZnCo2O4/polypyrrole nanofilm on QCM electrodes for ultrahighly sensitive humidity sensing application, Sensors Actuators, A Phys. 295 (2019) 687– 695.
- [59] W. Yan, D. Zhang, X. Liu, X. Chen, C. Yang, Z. Kang, Guar Gum/Ethyl Cellulose-Polyvinyl Pyrrolidone Composite-Based Quartz Crystal Microbalance Humidity Sensor for Human Respiration Monitoring, ACS Appl. Mater. Interfaces. 14 (2022) 31343–31353.
- [60] D. Zhang, R. Mao, X. Song, D. Wang, H. Zhang, H. Xia, Y. Ma, Y. Gao, Humidity sensing properties and respiratory behavior detection based on chitosan-halloysite nanotubes film coated QCM sensor combined with support vector machine, Sensors Actuators B Chem. 374 (2023) 132824.
- [61] R.J. Lazarowich, P. Taborek, B.Y. Yoo, N. V. Myung, Fabrication of porous alumina on quartz crystal microbalances, J. Appl. Phys. 101 (2007) 104909.
- [62] I. Goubaidoulline, G. Vidrich, D. Johannsmann, Organic vapor sensing with ionic liquids entrapped in alumina nanopores on quartz crystal resonators, Anal. Chem. 77 (2005) 615–619.
- [63] P. Pilla, A. Cusano, A. Cutolo, M. Giordano, G. Mensitieri, P. Rizzo, L. Sanguigno, V. Venditto, G. Guerra, Molecular sensing by nanoporous crystalline polymers, Sensors. 9 (2009) 9816–9857.
- [64] M.R. Eslami, N. Alizadeh, Ultrasensitive and selective QCM sensor for detection of trace amounts of nitroexplosive vapors in ambient air based on polypyrrole—Bromophenol blue nanostructure, Sensors Actuators B Chem. 278 (2019) 55–63.
- [65] M. Kikuchi, S. Shiratori, Quartz crystal microbalance (QCM) sensor for CH3SH gas by using polyelectrolyte-coated sol--gel film, Sensors Actuators B Chem. 108 (2005) 564–571.
- [66] D.I. Kim, R.H. Jeong, J.W. Lee, S. Park, J.-H. Boo, A highly sensitive quartz crystal microbalance sensor assisted with ZnO nanosheets for nerve agent detection, Funct. Mater. Lett. 14 (2021) 2151020.
- [67] Q. Zhou, L. Zhu, C. Zheng, J. Wang, Nanoporous Functionalized WS2/MWCNTs Nanocomposite for Trimethylamine Detection Based on Quartz Crystal Microbalance Gas Sensor, ACS Appl. Mater. \& Interfaces. 13 (2021) 41339–41350.
- [68] T. Sonklin, D. Munthala, S. Suksaweang, P. Janphuang, S. Pojprapai, Effect of Surface

- Modified Quartz Crystal Microbalance (QCM) on Detection Sensitivity for Prostate Specific Antigen (PSA), Integr. Ferroelectr. 222 (2022) 93–101.
- [69] K.M.M. Kabir, D. Jampaiah, A.E. Kandjani, M. Mullett, J. Tardio, Y.M. Sabri, S.K. Bhargava, Cold vapor integrated quartz crystal microbalance (CV-QCM) based detection of mercury ions with gold nanostructures, Sensors Actuators B Chem. 290 (2019) 453–458.
- [70] M. Lee, C. Yim, S. Jeon, Characterization of underwater stability of superhydrophobic surfaces using quartz crystal microresonators, Langmuir. 30 (2014) 7931–7935.
- [71] M. Lee, C. Yim, S. Jeon, Highly stable superhydrophobic surfaces under flow conditions, Appl. Phys. Lett. 106 (2015).
- [72] X. Chi, R. Zhang, T. Zhao, X. Gong, R. Wei, Z. Yin, H. Lin, D. Li, H. Shan, J. Gao, Targeted arsenite-loaded magnetic multifunctional nanoparticles for treatment of hepatocellular carcinoma, Nanotechnology. 30 (2019) 175101.
- [73] S. Baek, W. Kim, S. Jeon, K. Yong, Developing a non-optical platform for impact dynamics analysis on nanostructured superhydrophobic surfaces using a quartz crystal microbalance, Sensors Actuators B Chem. 262 (2018) 595–602.
- [74] I. Goubaidoulline, J. Reuber, F. Merz, D. Johannsmann, Simultaneous determination of density and viscosity of liquids based on quartz-crystal resonators covered with nanoporous alumina, J. Appl. Phys. 98 (2005) 14305.
- [75] R.J. Lazarowich, Phase behavior of helium in porous media, University of California, Irvine, 2006.
- [76] M. Lee, C. Yim, S. Jeon, Communication: Anti-icing characteristics of superhydrophobic surfaces investigated by quartz crystal microresonators, J. Chem. Phys. 142 (2015).
- [77] S. Liu, J. Tian, W. Zhang, Fabrication and application of nanoporous anodic aluminum oxide: a review, Nanotechnology. 32 (2021) 222001.
- [78] C. Mijangos, R. Hernández, J. Martin, A review on the progress of polymer nanostructures with modulated morphologies and properties, using nanoporous AAO templates, Prog. Polym. Sci. 54 (2016) 148–182.
- [79] J. Wang, Z. Li, Z. Gu, A comprehensive review of template-synthesized multi-component nanowires: From interfacial design to sensing and actuation applications, Sensors and Actuators Reports. 3 (2021) 100029.
- [80] N.L. Torad, S. Zhang, W.A. Amer, M.M. Ayad, M. Kim, J. Kim, B. Ding, X. Zhang, T. Kimura, Y. Yamauchi, Advanced nanoporous material--based QCM devices: A new horizon of interfacial mass sensing technology, Adv. Mater. Interfaces. 6 (2019) 1900849.
- [81] Q. Wei, Y. Fu, G. Zhang, D. Yang, G. Meng, S. Sun, Rational design of novel nanostructured arrays based on porous AAO templates for electrochemical energy storage and conversion, Nano Energy. 55 (2019) 234–259.
- [82] S.K. Hwang, S.H. Jeong, H.Y. Hwang, O.J. Lee, K.H. Lee, Fabrication of Highly Ordered Pore Array in Anodic Aluminum Oxide, Korean J. Chem. Eng. 19 (2002) 467–473.

- [83] K.K. Kanazawa, J.G. Gordon, Frequency of a quartz microbalance in contact with liquid, Anal. Chem. 57 (1985) 1770–1771.
- [84] K.K. Kanazawa, J.G. Gordon, The oscillation frequency of a quartz resonator in contact with liquid, Anal. Chim. Acta. 175 (1985) 99–105.
- [85] S.J. Martin, V.E. Granstaff, G.C. Frye, Characterization of a Quartz Crystal Microbalance with Simultaneous Mass and Liquid Loading, Anal. Chem. 63 (1991) 2272–2281.
- [86] K. Nielsch, F. Müller, A.P. Li, U. Gösele, Uniform nickel deposition into ordered alumina pores by pulsed electrodeposition, Adv. Mater. 12 (2000) 582–586.
- [87] J.R. ed. Rumble, ed., Hanbook of Chemistry and Physics 102nd Edition, 102nd ed., CRC press/Taylor & Francis, Boca Raton, FL, 2021.
- [88] A. Volk, C.J. Kähler, Density model for aqueous glycerol solutions, Exp. Fluids. 59 (2018) 75.
- [89] 3M, Technical Data 3M Novec 7000 Engineered Fluid, (2015) 1–6.
- [90] M.P. Proenca, C.T. Sousa, D.C. Leitao, J. Ventura, J.B. Sousa, J.P. Araujo, Nanopore formation and growth in phosphoric acid Al anodization, J. Non. Cryst. Solids. 354 (2008) 5238–5240.
- [91] C.T. Sousa, D.C. Leitao, M.P. Proenca, J. Ventura, A.M. Pereira, J.P. Araujo, Nanoporous alumina as templates for multifunctional applications, Appl. Phys. Rev. 1 (2014) 031102.